

Article

Changes of Inundation Frequency in the Yellow River Delta and Its Response to Wetland Vegetation

Yaoshen Fan ¹, Shoubing Yu ¹, Jinghao Wang ¹, Peng Li ², Shenliang Chen ², Hongyu Ji ², Ping Li ³
and Shentang Dou ^{1,*}

¹ Key Laboratory of Yellow River Channel and Estuary Regulation of the Ministry of Water Resources, Yellow River Institute of Hydraulic Research, Zhengzhou 450003, China

² State Key Laboratory of Estuarine and Coastal Research, East China Normal University, Shanghai 200241, China

³ First Institute of Oceanography, Ministry of Natural Resources, Qingdao 266061, China

* Correspondence: doushentang@hotmail.com

Abstract: The spatiotemporal changes of inundation frequency in the Yellow River Delta (YRD) have profound influences on sustainable ecological protection and are also closely relevant to economic development scarcity on the coast of China. However, long-term changes of inundation frequency have remained poorly characterized. Using the Google Earth Engine (GEE) cloud platform, this study processed Landsat images to explore inundation frequency changes from 1990 to 2020 in the YRD. The results indicated that (1) The existing water index combining the classification results based on the MLM (Maximum Likelihood Method) is suitable for the mapping of the long-term water bodies, especially in the coastal regions; (2) The inundation frequency showed a clearly uneven temporal–spatial distribution. The low inundation area (LIA) is mainly intertidal natural wetlands with a declining trend, while the high inundation area (HIA) is dominated by constructed wetlands with a rising trend; (3) The use frequency of artificial ponds determines the inundation frequency of the constructed wetland. The industry development has gradually matured, causing the inundation frequency from dispersion to concentration in the constructed wetland; and (4) In the natural wetland, the LIA have increased since 2010 and have accounted for 30% in 2020. The large-scale appearance of LIA occurs with the emergence of high vegetation abundance. *Spartina alterniflora* salt marshes with strong reproductive ability and high abundance lead to the difficulty of wetland flooding and reduce the inundation frequency.

Keywords: coastal wetland; Landsat image; Google Earth Engine; nature-based solutions



Citation: Fan, Y.; Yu, S.; Wang, J.; Li, P.; Chen, S.; Ji, H.; Li, P.; Dou, S. Changes of Inundation Frequency in the Yellow River Delta and Its Response to Wetland Vegetation. *Land* **2022**, *11*, 1647. <https://doi.org/10.3390/land11101647>

Academic Editors: Zhenguo Niu, Bin Zhao, Zhaoqing Luan and Bo Guan

Received: 22 August 2022

Accepted: 20 September 2022

Published: 23 September 2022

Publisher's Note: MDPI stays neutral with regard to jurisdictional claims in published maps and institutional affiliations.



Copyright: © 2022 by the authors. Licensee MDPI, Basel, Switzerland. This article is an open access article distributed under the terms and conditions of the Creative Commons Attribution (CC BY) license (<https://creativecommons.org/licenses/by/4.0/>).

1. Introduction

Coastal wetlands, which lie between the land and the ocean, are threatened from both human activity and natural hazards, such as climate change, sea level rise, local subsidence, decreased sediment supply, and harmful invasion [1–4]. Under those impacts, coastal wetland areas have been losing biodiversity and productivity has been diminishing [5]. The changes of wetland ecological pattern are directly reflected in the inundation frequency, which is the most important hydrological factor affecting the wetland ecosystem [6,7]. Therefore, it is of great significance to identify the spatial distribution and temporal variation characteristics of inundation frequency, and then reveal its impact on the distribution and succession of the wetland ecosystem.

Earlier work on detecting the spatial and temporal changes of flood inundation areas has been carried out, with some studies focusing on delineating wetlands in order to map the actual inundation extent, timing, and intensity for them to be able to understand floodplain vegetation dynamics [8–12], whereas others assessed the damage brought about by floods in urban areas [13–18]. To achieve their goals, they required a tool that was more effective and accurate than the collection of in situ field data, because some wetlands

were large and inaccessible. Recently, the Google Earth Engine (GEE) has enabled much wider access to satellite image time series, along with the capacity to process and analyze geospatial data [19–21]. So far, the GEE has been widely used, including mapping of built-up areas [22,23], crops [24,25], and wetlands [26,27], as well as open-surface water bodies [28–30]. Therefore, the GEE gives us a new insight to investigate the inundation dynamics in the river delta area.

The Yellow River Delta (YRD) has the youngest and most complete tidal wetlands in China [31]. There were a few studies about the losses of tidal wetlands in the YRD. For example, Fan et al. [32] found that reclamation and manipulation in eroded coasts strongly constrains the potential for wetland retreat to higher elevations. Other studies paid more attention to the distribution of natural wetlands and its driving factors [33,34]. However, due to the changes of wetland pattern, the inundation frequency experienced remarkable changes in this area, which also need to be explored. In general, few studies paid attention to the dynamics of inundation for the whole YRD using high-resolution Landsat images.

Thus, the objectives of this study are: (1) proposing a new framework to map inundation frequency of YRD in the GEE platform; (2) applying this method for analyzing the long-term dynamics of inundation frequency in the wetland ecosystem from 1990 to 2020; and (3) discussing the response relationship between wetland vegetation and changes of inundation frequency. Furthermore, the study can promote the development of coastal wetland protection in the YRD.

2. Materials and Methods

2.1. Study Area

The YRD is located on the northern coast of China adjacent to the Bohai Sea and one of the largest estuarine deltas in the world [35,36]. The main body of the YRD is located in Dongying City, Shandong Province [37]. In order to accurately grasp the boundary of the Delta, this paper takes the administrative boundary of Dongying City as the land boundary of the YRD (Figure 1a,b).

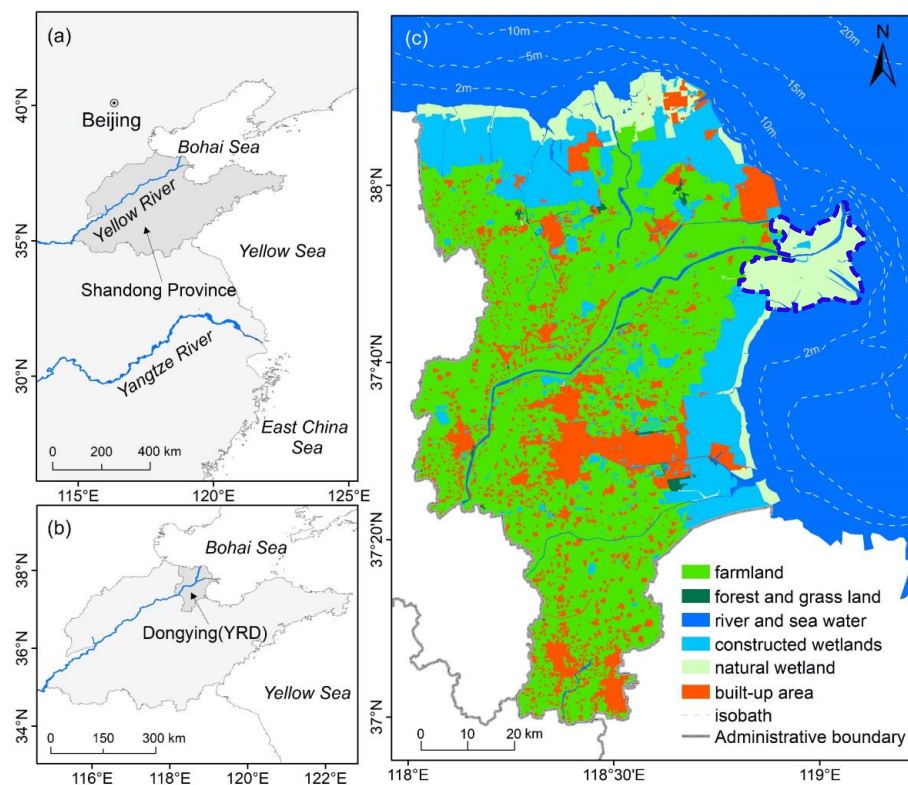


Figure 1. (a,b) Geographic location of the Yellow River Delta (YRD). (c) Land use in the YRD, and the active estuarine area is circled by the blue dotted line.

Based on the Landsat remote sensing image on 17 July 2020 and combined with the field survey, we obtained the latest land use in the study area, as shown in Figure 1c. Coastal wetlands in the Yellow River Delta can be divided into natural wetlands and constructed wetlands. Natural wetlands are concentrated below the high tide line at a lower altitude, mainly herbaceous swamps and shrub swamps, of which the dominant species are *Phragmites australis*, *Suaeda salsa*, and *Spartina alterniflora*. The mid altitude areas between industrial and agricultural land (farmland and construction land) and the natural wetlands are constructed wetlands, produced by human reclamation activities, such as aquaculture ponds and salt ponds. According to statistics, the area of natural wetlands reaches 1000 km², accounting for 12.1% of the land area of Dongying, and the area of constructed wetlands reaches 1300 km², accounting for 15.7%.

2.2. Data

To acquire more information of the inundation frequency, this study used a dense time series of Landsat images of the entire YRD, including all available Landsat 5, 7, and 8 images. Complete coverage of the study area is achieved with one tile (path 121, row 34) of the Landsat Worldwide Reference System (WRS). In this study, a total of 2343 of these images was 306, including 42 from 1989 to 1991, 53 from 1999 to 2001, 51 from 2009 to 2011, and 67 from 2019 to 2021 respectively for the water bodies extracted for 1990, 2000, 2010, and 2020. Detailed statistical information about the Landsat Thematic Mapper (TM), Enhanced Thematic Mapper (ETM+), and Operational Land Imager (OLI) data used in this study is given in Table 1.

Table 1. Properties of remote sensing selected used in this study.

Period	Sensor	Time	Image Count
1990	Landsat 5 TM	From 1 January 1989 to 31 December 1991	42
2000	Landsat 5 TM Landsat 7 ETM+	From 1 January 1999 to 31 December 2001	53
2010	Landsat 5 TM Landsat 7 ETM+	From 1 January 2009 to 31 December 2011	51
2020	Landsat 5 TM Landsat 7 ETM+ Landsat 8 OLI	From 1 January 2019 to 31 December 2021	67

Moreover, GF-1/2 images were used to evaluate the accuracy of the extracted surface water bodies. GF-2 imaged on 1 March 2019 and GF-1 imaged on 16 July 2020 were used to deploy edge-points for confusion matrix [38]. GF-2 and GF-1 images were radiometrically calibrated and atmospherically corrected by ENVI software, and fused with their panchromatic bands to generate 1 m and 2 m resolution multispectral images, respectively.

2.3. Methods

2.3.1. Water Body Extraction and Assessment

To extract the water bodies, several imaging systems were employed. The Normalized Difference Water Index (NDWI) provides a greater accuracy and has been demonstrated in highly turbid coastal areas. It has been used in the tidal flats of Bohai Rim [39], the tidal flats along the Jiangsu coast [40], and other intertidal regions across East Asia [41]. Therefore, it was adopted in the study. The formulation of NDWI is expressed in the equation: $NDWI = (G - Ni)/(G + Ni)$, where “G” represents the green light band and “Ni” represents the near-infrared band.

The extraction of water bodies was supported by the GEE cloud platform [28,29]. Firstly, for each image, the cloud, cloud shadow, and snow/ice were corrected by Landsat quality band generated by the Fmask algorithm [42]. Then, the NDWI was applied to obtain a preliminary mapping of water bodies. Moreover, the Maximum Likelihood Method (MLM) was used to calibrate and classify the remote sensing image data, and

two surface types of water and vegetation are obtained. Combining the classification results of NDWI and MLM, the final water bodies were obtained. The results of the image classification make up for the defect of image pure end member selection, which has more advantages in the water land interaction area and is more in line with the actual situation of the YRD.

Confusion matrix is a commonly used classification accuracy evaluation method, and it displays the number of correctly classified objects and the wrong categories in the form of a matrix [43]. In order to express the overall accuracy of the classification results, the confusion matrix derives two indicators: the overall classification accuracy and kappa coefficient. The overall classification accuracy refers to the ratio of the number of correctly classified categories to the number of total categories, which represents the overall classification consistency degree in the error matrix, but its stability is affected by the imbalance of the number of samples in each category. Kappa coefficient refers to the proportion of error reduction between classification results and completely random classification, indicating the degree of coincidence between actual categories and classification results.

2.3.2. Change Analysis of Water Bodies

The Water Body Frequency (*WBF*) of each pixel can be calculated from the following:

$$WBF = \frac{\sum_{i=1}^N w}{N} \times 100\% \quad (1)$$

where N indicates the number of all the good observations in a specific period, and w is a binary variable. *WBF* ranges from 0% to 100%. According to *WBF*, inundation frequency in the YRD can be divided into three types: long-term inundation frequency ($WBF > 70\%$), mid-term inundation frequency ($20\% < WBF \leq 70\%$), and short-term inundation frequency ($WBF \leq 20\%$). The areas covered by long-term water bodies are defined as high inundation areas (HIA), the areas covered by mid-term water bodies are defined as medium inundation areas (MIA), and the areas covered by short-term water bodies are defined as low inundation areas (LIA).

2.3.3. Vegetation Distribution Response

Vegetation biomass can be expressed by vegetation distribution area and vegetation fractional coverage, namely vegetation abundance. Integrated with the changes of vegetation abundance, which were extracted based on Linear Spectral Mixture Analysis (LSMA) [44], we further discuss the response of inundation frequency to the vegetation development.

LSMA is a method physically based on image processing, assuming that spectrum measured by a sensor is a linear combination of the spectra of all components within the pixel, and can be expressed as:

$$R_i = \sum_{k=1}^n f_k R_{ik} + ER_i \quad (2)$$

where $i = 1, \dots, m$ (number of spectral bands); $k = 1, \dots, n$ (number of endmembers); R_i is the spectral reflectance of band i which contains one or more endmembers; f_k is the proportion of endmember k within the pixel; R_{ik} is the known spectral reflectance of endmember k within the pixel on band i ; and ER_i is the error for band i . Root mean square was used to measure the accuracy of solution:

$$RMS = \sqrt{(\sum_{i=1}^m ER_i^2) / m} \quad (3)$$

From Equation (3), we can see that the smaller the *RMS* is, the smaller the error will be. Selecting suitable endmembers is the key factor determining the overall accuracy during the unmixing process. As the spectral information of delta land cover is so complicated, and atmosphere also influences the spectra in addition, image endmembers can give a

higher accuracy. Thus, in this study, image endmembers were chosen and derived from the Landsat TM/ETM+ image, based on geometric vertices.

The plants in YRD wetland are at their most thriving from the end of September to the beginning of October every year [45]. Considering that the growth of wetland vegetation is not only affected by water inundation, but also controlled by its own seasonal growth rhythm, the vegetation abundance value in the corresponding research period is calculated based on the remote sensing image in October. All in all, the workflow of this study is shown Figure 2.

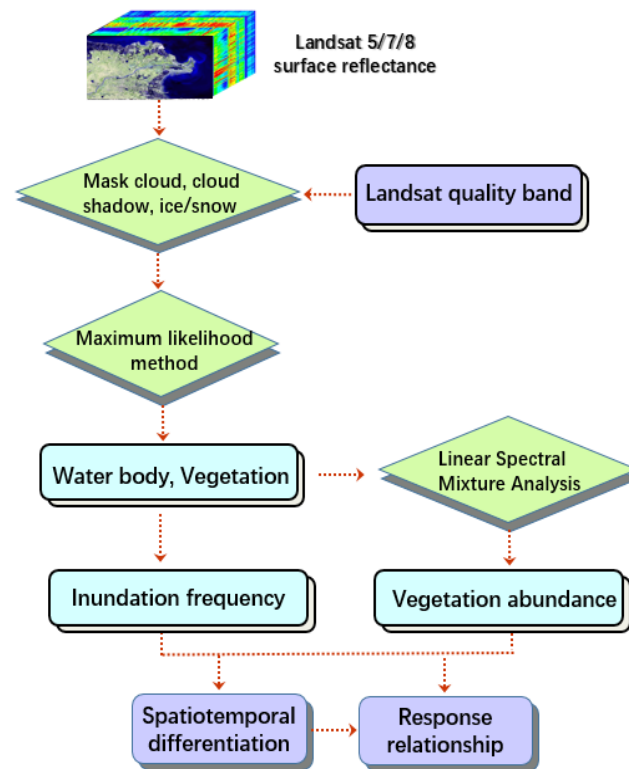


Figure 2. The flowchart of the extraction of surface water bodies and vegetation abundance in the YRD.

3. Results and Discussion

3.1. Accuracy Assessment

The reference samples consisted of two categories, water and non-water, as the focus of this study is the spatio-temporal dynamics of surface water. In the GF-1/2 images, 1000 test samples, including 505 water samples and 495 non-water samples, were randomly generated. Based on this, the confusion matrix of accuracy assessment was established. Table 2 shows the accuracy. The user accuracy and producer accuracy have reached above 95%, and the overall accuracy and kappa coefficient was 96.89% and 0.934, respectively. The results showed that the detected water products in the YRD had higher accuracy and then can be used for further analysis.

Table 2. The confusion matrix for accuracy assessment.

Samples	GF-1/2		Total	User's Accuracy	
	Water	Non-Water			
Landsat	Water	492	13	505	97.43%
	Non-water	18	477	495	96.36%
	Total	510	490	1000	Overall accuracy = 96.89
	Producer's accuracy	96.47%	97.35%		Kappa coefficient = 0.934

3.2. Dynamics of Inundation Frequency

3.2.1. The Mapped Inundation Frequency

Based on above-mentioned methods, we produced maps of inundation frequency in the YRD for the years 1990, 2000, 2010, and 2020. As shown in Figure 3, the blue bar indicates the area of the inundation area. The darker the color, the higher the inundation frequency, and the lighter the color, the lower the inundation frequency. All other non-inundation regions are masked off in white.

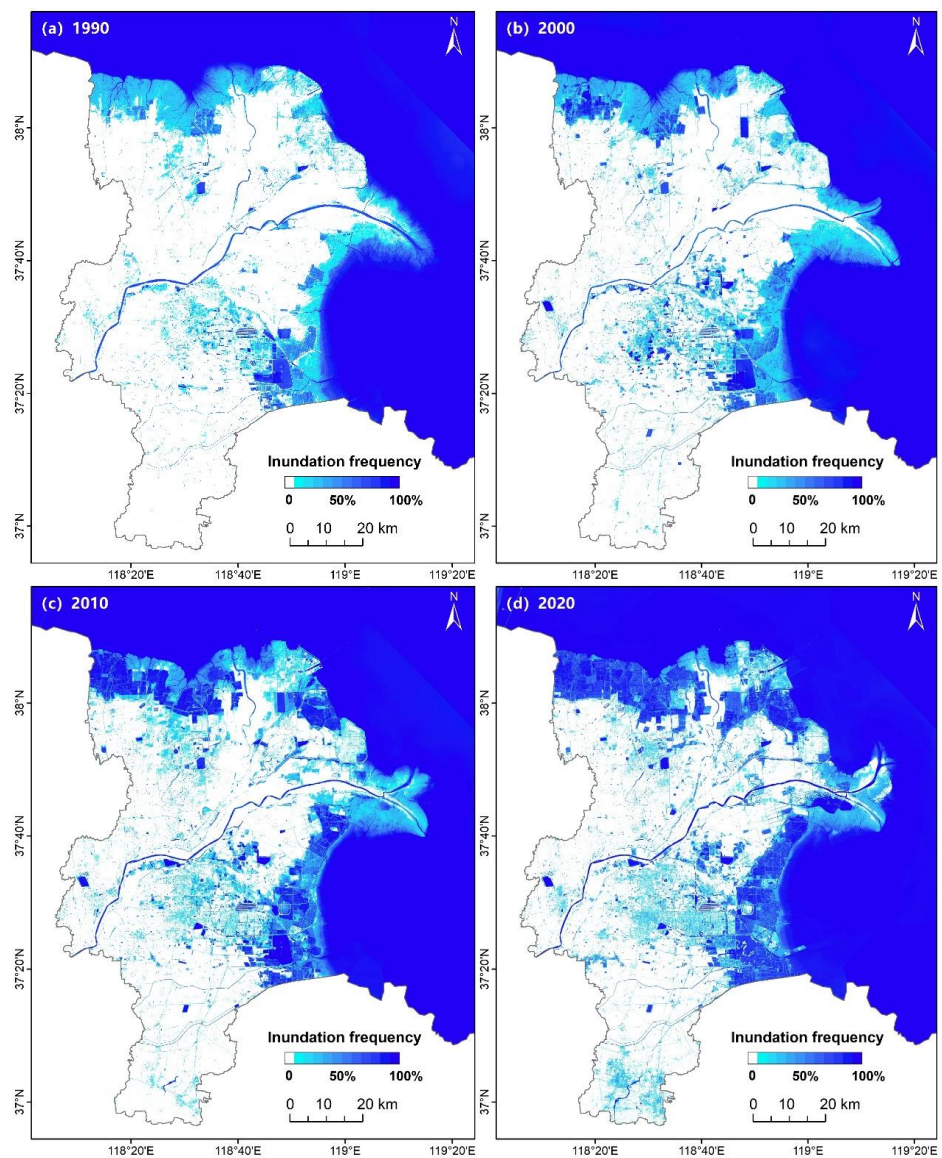


Figure 3. The spatial extent of different inundation area of (a) 1990, (b) 2000, (c) 2010, and (d) 2020 in the YRD.

The inundation frequency in the YRD showed a clearly uneven temporal–spatial distribution. Generally speaking, the LIA is mainly the intertidal natural wetland and the impervious surface of urban construction land. In addition to the sea area, the HIA also includes rivers, lakes, reservoirs, and constructed wetlands. With the development of urbanization and human construction, the areas of low inundation frequency expand from coastal low-altitude intertidal zones to inland urban construction areas where the diffusion trends of the HIA appearing in the low-altitude intertidal zone are very obvious.

3.2.2. Area Changes of HIA and MLIA

The erosion and accretion areas along the YRD coast are important factors causing the change of inundation frequency. Newly deposited land develops into coastal wetlands, which usually covers intermittent water bodies. The sea water brought by coastal erosion invades the land, making the MIA or LIA turn into long-term water bodies. Therefore, the accretion area can be regarded as the transformation from HIA to MLIA (Combined name of MIA and LIA), and the erosion area can be regarded as reverse transformation. For more accurate statistics, we analyzed and calculated the change of coastal erosion and accretion areas in each period (Figure 4) respectively, as the MLIA to be added and the HIA to be subtracted, and obtained corrected area, namely $MLIA_c$ and HIA_c . The shoreline used to calculate erosion and accretion area was extracted from the Landsat images of the corresponding year.

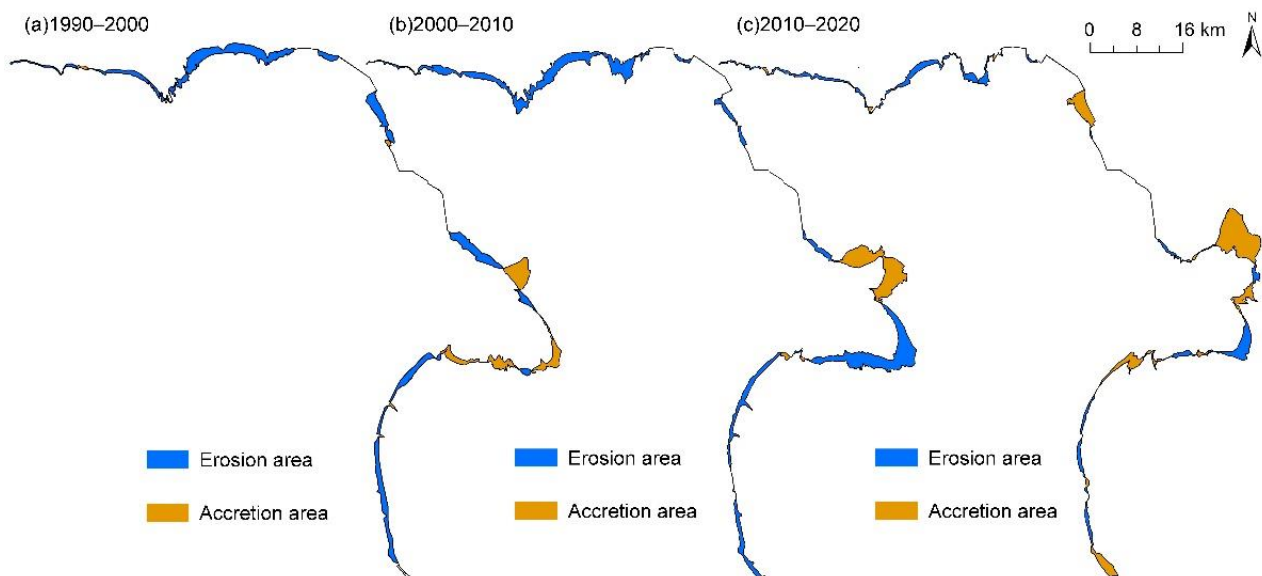


Figure 4. The erosion and accretion area along the YRD coast during different periods.

The area change curves of MLIA and HIA are shown in Figure 5a, including before and after correction. Although their overall change trend has not changed before and after correction, the period of 2010~2020 needs our focus. During this period, MLIA decreased slightly before correction, from 5069 km² to 5034 km², but changed to an increasing trend after correction, from 5164 km² to 5218 km². This shows that the trend of MLIA in this period can be attributed to the coastal erosion and accretion.

In terms of the proportion in the total water body area, $MLIA_c$ accounted for 55.25% in 1990. With the passage of time, its proportion experienced decreased continuously, with 40.76% in 2020 (Figure 5c). The proportion of HIA_c experienced continues to increase, from 44.75% in 1990 to 59.24% in 2020. An important reason for the opposite trend is the artificial reclamation in the natural wetland. Reclamation activities converted natural wetlands that were originally short-term or medium-term inundation areas into constructed wetlands, such as aquaculture ponds and salt ponds. As shown in Figure 5a,b, the change trend of the proportion of natural wetlands and constructed wetlands is consistent with that of $MLIA_c$ and HIA_c . The feature of these constructed wetlands is the need for continuous water storage to ensure their efficient economic value. During 2000–2010, the proportion of natural wetlands decreased, and the proportion of constructed wetlands increased the most (Figure 5b). Our previous research work also shows that the reclamation activity was the fastest during this period [32]. This fact explains that the changes of $MLIA_c$ and HIA_c were the largest during 2000–2010. In addition, with the implementation of the saline alkali land transformation project in the YRD, some saline-alkali land has been transformed into

fishery breeding land [46,47], resulting in the transformation of the non-water area into long-term water bodies and the significant increase of HIA_c.

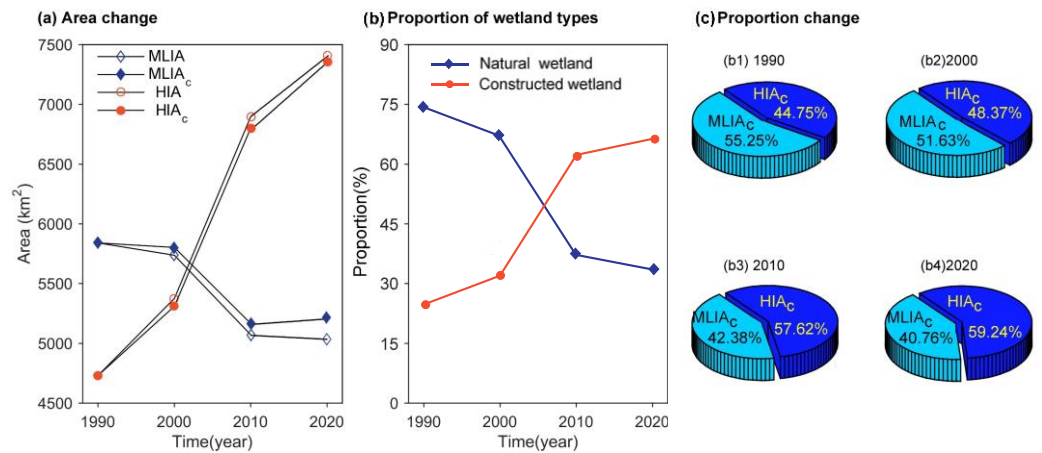


Figure 5. The area and proportion change of different inundation frequency and wetland landscapes in the YRD from 1990 to 2020. (a) The area of MLIA, MLIA_c, HIA, and HIA_c. (b) The proportion change of natural and constructed wetlands. (c) The proportion of MLIA_c and HIA_c.

3.3. Inundation Frequency in Wetland Ecosystem

In this study, the pixel size of the remote sensing image is unified as 30 × 30 m². Therefore, the number of pixels with different inundation frequencies represents the area with different inundation frequencies. According to the changes of the number of pixels in natural wetland and constructed wetland, we can observe the dynamic change characteristics and laws of wetland. The spatial distribution information of natural wetland and constructed wetland was interpreted from the Landsat images of the corresponding years. As shown in Figure 6, each color bar from left to right represents the inundation frequency from 0 to 100%. The light and dark of the color bar represents the number of pixels. The darker the red represents the more corresponding pixels, which gradually changes to yellow, light blue and dark blue, representing the decrease of the number of pixels.

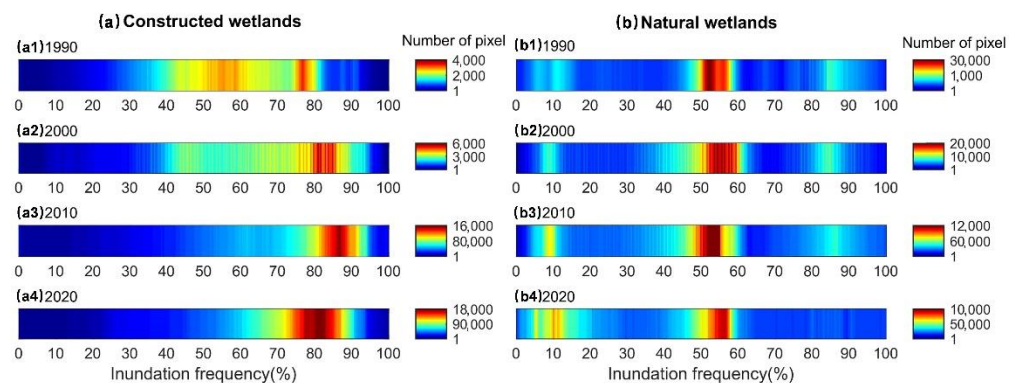


Figure 6. The inundation frequency distribution of wetlands in the YRD from 1999 to 2020, (a) constructed wetlands and (b) natural wetlands.

3.3.1. Constructed Wetland

For its high economic production value, constructed wetlands should be dominated by high inundation areas, but the inundation frequency of constructed wetlands in the YRD is in dynamic change. Its overall trend gradually changed from dispersion to high inundation concentration (Figure 6a). In 1990 and 2000, the inundation frequency distribution span was in the range of 40~90%, while in 2010 and 2020, the inundation frequency was concentrated in the range of 70~90%.

The constructed wetlands in the YRD are mainly coastal aquaculture ponds and salt drying ponds. The use frequency of these artificial buildings determines the inundation frequency of the constructed wetlands. Their use frequency is related to the development and perfection of the industry. The change of aquaculture products per unit area can spy on the development degree of aquaculture industry. From the change of aquaculture products per unit area, the development degree of aquaculture industry can be clarified. According to the data published in the statistical yearbook of Dongying City, the amount of seawater aquaculture yield per unit area has gradually stabilized at about 3 t/ha after 2005 (Figure 7a), and the amount of freshwater aquaculture yield per unit area has gradually stabilized at about 4 t/ha after 2009 (Figure 7b). It can be seen that the period of 1990~2010 is the development stage of aquaculture industry in the YRD. During this period, some aquaculture ponds have been completed and used for water injection, while some are under construction and not put into use. Naturally, the use frequency is high and low, resulting in scattered inundation frequency. After 2010, the stable amount of aquaculture products per unit area means that the aquaculture industry has developed maturely, and the inundation frequency is relatively concentrated in a small range.

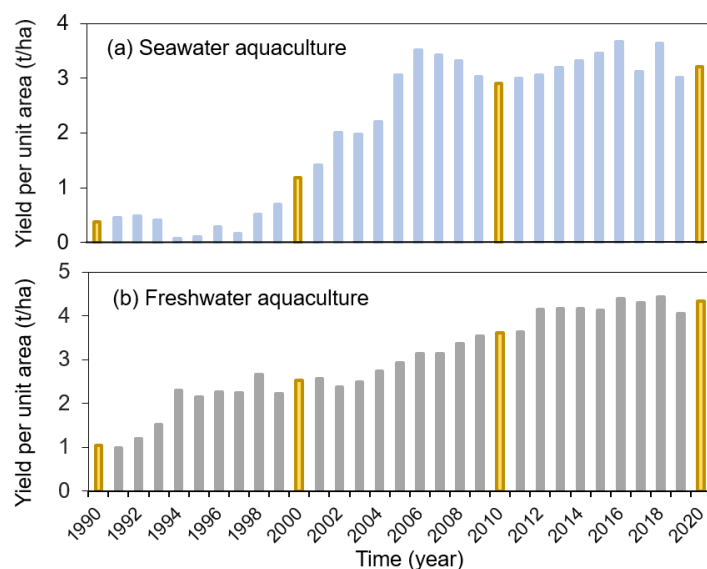


Figure 7. Changes of aquaculture yield per unit area in Dongying City from 1990 to 2021. The yellow columns represent the years of the study, 1990, 2000, 2010 and 2020.

3.3.2. Natural Wetland

There are three color highlighted areas of natural wetland inundation frequency (Figure 6b), which are located in 5~15%, 45~60%, and 80~90% respectively. The 45~60% inundation area accounts for the largest proportion over the years. It shows that the natural wetland is dominated by mid-term water bodies, with a small area of short- and long-term water bodies.

From the distribution of inundation frequency over the years, we observe that the inundation frequency has both a change zone and a stable zone. The stable zone is the MIA, accounting for 60~80%, which is the core area with the most stable vegetation growth in the natural wetland ecosystem. The change zone is the relatively small proportion of LIA and HIA. This too shows the opposite trend, that is, the former shows an upward trend and the latter shows a downward trend. The wetland inundation frequency map from 1990 to 2000 (Figure 3a–c) shows that the HIA is mainly the salt marsh area near the sea-land boundary. This area, namely the lower intertidal zone, is strongly affected by tidal inundation [48], so it has become a long-term water body naturally. From 2010 to 2020, the proportion of HIA decreased significantly, while the proportion of LIA increased. To 2020, the proportion of LIA has reached a certain scale, accounting for 30% of the total area of natural wetlands. The wetland inundation frequency diagram (Figure 3d) reveals a phenomenon worthy of

focus, that is, the low inundation area expanded in 2020 is mainly located in the lower intertidal zone near the current estuary, and even a large area of no-water body appears.

3.4. Response to Vegetation Distribution

The reasons for the large-scale appearance of LIA in natural wetlands are either the change of water volume or are related to the habitat change of natural wetlands. The amount of water entering and then flooding the wetland is determined by the river discharge and the change of sea level. We selected the daily average flow of Lijin Station ($118^{\circ}19'31.65''$ E, $37^{\circ}33'27.74''$ N) on the Yellow River to represent the amount of water entering the sea or wetland, and selected the multi-year daily average tide level value of Gudong Station ($119^{\circ}4'34.54''$ E, $37^{\circ}56'31.21''$ N) to represent the sea level, and compared the changes of the two values in different years. The large discharge processes in 2010 and 2020 shown in the box diagram are significantly more than those in 1990 and 2000 (Figure 8a). The daily average tide level of Gudong Station also shows a stable trend (Figure 8b). It can be seen that the water volume is not the main reason for the large number of low inundation areas in natural wetlands.

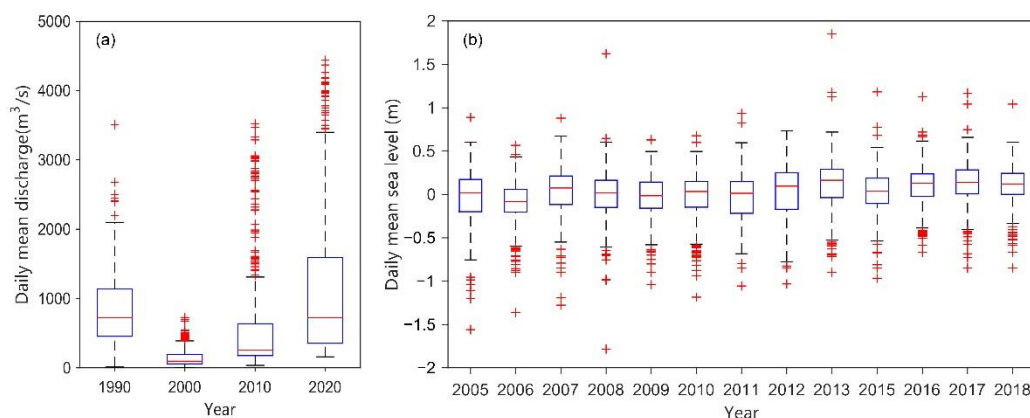


Figure 8. (a) Box chart of river discharge of Lijin Station from 1990 to 2020, and (b) box chart of daily average tide level of Gudong Station from 2005 to 2018.

In order to explore the impact of wetland habitat changes on the expansion of LIA in natural wetlands, we compared the relationship between vegetation abundance and inundation frequency in the active estuarine area (see Figure 1c for the scope). From the scatter diagram of inundation frequency and vegetation abundance (Figure 9), it can be seen that there is a certain correlation between them. The higher the inundation frequency, the lower the corresponding vegetation abundance. In 1990 and 2000, the inundation frequency was concentrated at 45~60%, and the corresponding vegetation abundance was between 45~55. In 2010, 5~15% of the low inundation areas began to appear large, and its corresponding vegetation abundance was more than 60. By 2020, the patches with high vegetation abundance corresponding to the low inundation frequency continued to expand.

The timing of the phenomenon that low inundation frequency corresponds to high vegetation abundance is highly consistent with the time of rapid propagation outbreak of *Spartina alterniflora* in this area. This fact makes us focus on the *Spartina alterniflora* salt marsh. This alien species was successfully introduced in the Yellow River Delta in the 1990s. During the 11 years from 1999 to 2010, the distribution range and area of *Spartina alterniflora* increased slowly [49]. After 2011, it began to enter the growth period of rapid spread, and quickly invaded the local coastal wetland habitat [50]. By 2020, it had a distribution area of 52.7 km² in the active estuarine area, accounting for 31% of the total salt marsh area [51]. Because *Spartina alterniflora* has strong stress resistance and reproductive ability, the salt marsh formed by it shows higher vegetation abundance. The sedimentary environment of salt marsh vegetation is dominated by vegetation mediated. This fact led the high vegetation abundance area to enhance local deposition and show better

elevation than areas with a low vegetation abundance area, which causes the inundation frequency of the former to be less than that of the latter. The analysis results of *Spartina alterniflora*, *Suaeda salsa*, and *Phragmites australis* also confirmed this phenomenon. The spatial distributions of the three types of vegetation were obtained by interpreting the Landsat image in 2020. There is a negative correlation between inundation frequency and vegetation abundance at each sample point of the three marshes (Figure 10), among which *Spartina alterniflora* salt marsh shows the best correlation ($R^2 = 0.68$). The sample with the highest vegetation abundance is in the *Spartina alterniflora* salt marsh area, with the lowest inundation frequency, concentrated in 5~25%. The inundation frequency and vegetation abundance span of *Suaeda salsa* are significantly larger than the other two, but they contain the vast majority of samples, which shows samples with high inundation frequency and low vegetation abundance.

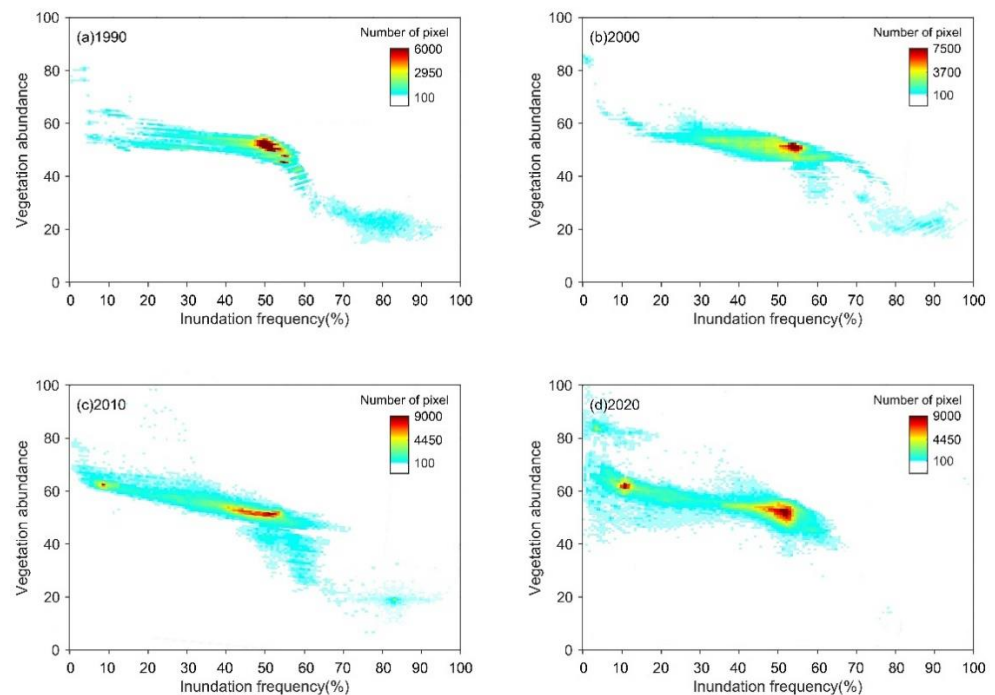


Figure 9. The inundation frequency versus vegetation abundance diagram in active estuarine area.

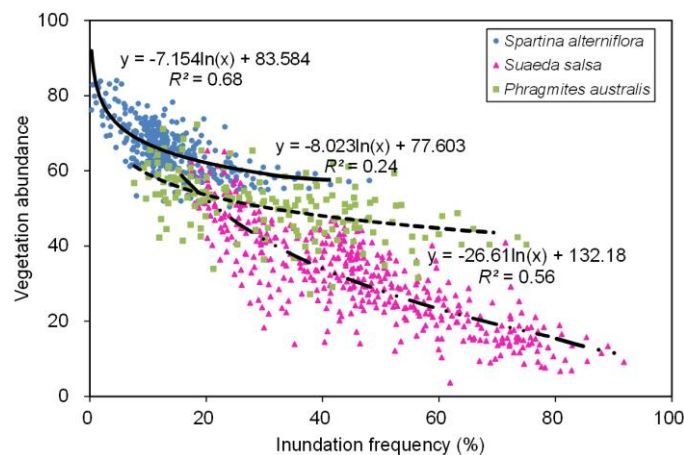


Figure 10. The relationship between inundation frequency and vegetation abundance of samples in three types of wetland vegetation.

From the perspective of vegetation distribution change, we have analyzed the internal mechanism of inundation frequency change in the natural wetland. For the YRD, the vege-

tation distribution is only a part of its dynamic changes [52,53], and more potential effects come from the morphodynamic changes under the action of estuarine hydrodynamics and the coupling between vegetation [54,55]. In the future, exploring biogeomorphology and further understanding the evolution mechanism of wetland habitats [56,57], including inundation changes, is an important way to protect this natural wetland that is constantly eroded by human activities and alien species.

4. Conclusions

In this study, we proposed a framework for long-term mapping of inundation frequency in the GEE platform. By clustering multiple water bodies within a 3-year period and using a percentile-based image composite method, we were able to produce maps of inundation frequency for the years 1990, 2000, 2010, and 2020 in the YRD.

The inundation frequency showed a clearly uneven temporal–spatial distribution in the YRD. The LIA is mainly the intertidal natural wetland and the urban construction land with a declining trend, and the HIA includes permanent water bodies (e.g., rivers, lakes, reservoirs) and constructed wetlands with a rising trend. In addition to coastal erosion and accretion, which can explain a small part of this phenomenon, this trend is mainly attributed to the artificial reclamation in the natural wetland. The use frequency of coastal aquaculture ponds and salt drying ponds determines the inundation frequency of the constructed wetland. The industry development has gradually matured, resulting in the inundation frequency from dispersion to concentration in the constructed wetland. Over the years, the inundation frequency is dominated by 45~60% in the natural wetland, while the LIA have increased since 2010 and have accounted for 30% of the total area of natural wetlands in 2020. The large-scale appearance of LIA is not isolated, but occurs with the emergence of high vegetation abundance. Compared with *Suaeda salsa* and *Phragmites australis*, *Spartina alterniflora* salt marsh showed the best correlation between vegetation abundance and inundation frequency. *Spartina alterniflora* with strong reproductive ability and high abundance vegetation enhances the local deposition and shows better elevation than other salt marshes, which eventually leads to the difficulty of wetland flooding and reduces the inundation frequency.

Author Contributions: Conceptualization, Y.F. and S.D.; methodology, S.Y.; software, P.L. (Peng Li); validation, H.J., J.W. and Y.F.; formal analysis, Y.F.; investigation, P.L. (Peng Li); resources, S.C.; data curation, S.C.; writing—original draft preparation, Y.F.; writing—review and editing, S.C.; visualization, J.W.; supervision, H.J.; project administration, H.J.; funding acquisition, Y.F., P.L. (Ping Li) and S.D. All authors have read and agreed to the published version of the manuscript.

Funding: This research was funded by the State Key Program of National Natural Science Foundation of China (NO. U2243207), the National Natural Science Foundation of China (No. 52079056), the Basic Scientific Research Project of YRIHR (No. HKY-JBYW-2020-06 and No. HKY-JBYW-2020-11) and the NSFC of Shandong Province (No. ZR2020MD063).

Data Availability Statement: The data that support the findings of this study are available on request from the corresponding author (S.D.).

Acknowledgments: We would like to thank GEE for providing Landsat imagery.

Conflicts of Interest: The authors declare no conflict of interest.

References

1. Kirwan, M.L.; Megonigal, J.P. Tidal wetland stability in the face of human impacts and sea-level rise. *Nature* **2013**, *504*, 53–60. [[CrossRef](#)] [[PubMed](#)]
2. Wu, W.; Zhi, C.; Gao, Y.; Chen, C.; Chen, Z.; Su, H.; Lu, W.; Tian, B. Increasing fragmentation and squeezing of coastal wetlands: Status, drivers, and sustainable protection from the perspective of remote sensing. *Sci. Total Environ.* **2022**, *811*, 152339. [[CrossRef](#)]
3. Liu, Z.Z.; Fagherazzi, S.; Cui, B.S. Success of coastal wetlands restoration is driven by sediment availability. *Commun. Earth Environ.* **2021**, *2*, 44. [[CrossRef](#)]
4. Acua-Piedra, J.F.; Quesada-Román, A. Multidecadal biogeomorphic dynamics of a deltaic mangrove forest in Costa Rica. *Ocean Coast. Manag.* **2021**, *211*, 105770. [[CrossRef](#)]

5. Schuerch, M.; Spencer, T.; Temmerman, S.; Kirwan, M.L.; Wolff, C.; Lincke, D.; McOwen, C.J.; Pickering, M.D.; Reef, R.; Vafeidis, A.T.; et al. Future response of global coastal wetlands to sea-level rise. *Nature* **2018**, *561*, 231–234. [[CrossRef](#)] [[PubMed](#)]
6. Coleman, A.M.; Diefenderfer, H.L.; Ward, D.L.; Borde, A.B. A spatially based area–time inundation index model developed to assess habitat opportunity in tidal–fluvial wetlands and restoration sites. *Ecol. Eng.* **2015**, *82*, 624–642. [[CrossRef](#)]
7. Liu, Z.Z.; Fagherazzi, S.; She, X.J.; Ma, X.; Xie, C.J.; Cui, B.S. Efficient tidal channel networks alleviate the drought-induced die-off of saltmarshes: Implications for coastal restoration and management. *Sci. Total Environ.* **2020**, *749*, 141493. [[CrossRef](#)]
8. Townsend, P.A.; Walsh, S.J. Modeling floodplain inundation using an integrated GIS with radar and optical remote sensing. *Geomorphology* **1998**, *21*, 295–312. [[CrossRef](#)]
9. Wolter, P.T.; Townsend, P.A.; Sturtevant, B.R.; Kingdon, C.C. Remote sensing of the distribution and abundance of host species for spruce budworm in northern Minnesota and Ontario. *Remote Sens. Environ.* **2008**, *112*, 3971–3982. [[CrossRef](#)]
10. Quesada-Román, A.; Ballesteros-Canovas, J.A.; Granados, S.; Birkel, C.; Stoffel, M. Dendrogeomorphic reconstruction of floods in a dynamic tropical river. *Geomorphology* **2020**, *359*, 107133. [[CrossRef](#)]
11. Box, W.; Jrvcl, J.; Vstl, K. Flow resistance of floodplain vegetation mixtures for modelling river flows. *J. Hydrol.* **2021**, *601*, 126593. [[CrossRef](#)]
12. Quesada-Román, A.; Villalobos-Chacón, A. Flash flood impacts of hurricane otto and hydrometeorological risk mapping in Costa Rica. *Geogr. Tidsskr. Dan. J. Geogr.* **2020**, *120*, 142–155. [[CrossRef](#)]
13. Takagi, H.; Ty, T.V.; Thao, N.D.; Esteban, M. Ocean tides and the influence of sea-level rise on floods in urban areas of the Mekong Delta. *J. Flood Risk Manag.* **2015**, *8*, 292–300. [[CrossRef](#)]
14. Takagi, H.; Tsurudome, C.; Thao, N.D.; Anh, L.T.; Ty, T.V.; Tri, V.P. Ocean tide modelling for urban flood risk assessment in the Mekong Delta. *Hydrol. Res. Lett.* **2016**, *10*, 21–26. [[CrossRef](#)]
15. Thanvisitthpon, N.; Shrestha, S.; Pal, I.; Ninsawat, S.; Chaowiwat, S. Assessment of flood adaptive capacity of urban areas in Thailand. *Environ. Impact Assess. Rev.* **2020**, *81*, 106363. [[CrossRef](#)]
16. Quesada-Román, A.; Liu, W.C. Disaster risk assessment of informal settlements in the Global South. *Sustainability* **2022**, *14*, 10261. [[CrossRef](#)]
17. Yereseme, A.K.; Surendra, H.J.; Kuntoji, G. Sustainable integrated urban flood management strategies for planning of smart cities: A review. *Sustain. Water Resour. Manag.* **2022**, *8*, 85. [[CrossRef](#)]
18. Quesada-Román, A. Flood risk index development at the municipal level in Costa Rica: A methodological framework. *Environ. Sci. Policy* **2022**, *133*, 98–106. [[CrossRef](#)]
19. Gorelick, N.; Hancher, M.; Dixon, M.; Ilyushchenko, S.; Thau, D.; Moore, R. Google Earth Engine: Planetary-scale geospatial analysis for everyone. *Remote Sens. Environ.* **2017**, *202*, 18–27. [[CrossRef](#)]
20. Adepoju, K.A.; Adelabu, S.A. Improving accuracy of Landsat-8 OLI classification using image composite and multisource data with Google Earth Engine. *Remote Sens. Lett.* **2020**, *11*, 107–116. [[CrossRef](#)]
21. Venkatappa, M.; Sasaki, N.; Han, P.; Abed, I. Impacts of droughts and floods on croplands and crop production in Southeast Asia—An application of Google Earth Engine. *Sci. Total Environ.* **2021**, *795*, 148829. [[CrossRef](#)] [[PubMed](#)]
22. Allen, R.G.; Tasumi, M.; Morse, A.; Trezza, R. A landsat-based energy balance and evapotranspiration model in Western US water rights regulation and planning. *Irrig. Drain. Syst.* **2005**, *19*, 251–268. [[CrossRef](#)]
23. Xu, J.; Xiao, W.; He, T.; Deng, X.Y.; Chen, W.Q. Extraction of built-up area using multi-sensor data—A case study based on Google Earth Engine in Zhejiang Province, China. *Int. J. Remote Sens.* **2021**, *42*, 389–404. [[CrossRef](#)]
24. Shaharum, N.; Shafri, H.; Wan, A.; Samsatli, S.; Al-Habshi, M.; Yusuf, B. Oil palm mapping over Peninsular Malaysia using Google Earth Engine and machine learning algorithms. *Remote Sens. Appl. Soc. Environ.* **2020**, *17*, 100287. [[CrossRef](#)]
25. Pan, L.; Xia, H.; Zhao, X.; Guo, Y.; Qin, Y.C. Mapping winter crops using a Phenology Algorithm, time-series Sentinel-2 and Landsat-7/8 images, and Google Earth Engine. *Remote Sens.* **2021**, *13*, 2510. [[CrossRef](#)]
26. Hird, J.; DeLancey, E.; McDermid, G.; Kariyeva, J. Google Earth Engine, Open-access satellite data, and machine learning in support of large-area probabilistic wetland mapping. *Remote Sens.* **2017**, *9*, 1315. [[CrossRef](#)]
27. Zhou, Y.; Dong, J.; Xiao, X.; Liu, R.G.; Zou, Z.H.; Zhao, G.; Ge, Q. Continuous monitoring of lake dynamics on the Mongolian Plateau using all available Landsat imagery and Google Earth Engine. *Sci. Total Environ.* **2019**, *689*, 366–380. [[CrossRef](#)]
28. Deng, Y.; Jiang, W.; Tang, Z.; Li, J.; Lv, J.; Chen, Z.; Jia, K. Spatio-temporal change of lake water extent in Wuhan urban agglomeration based on Landsat images from 1987 to 2015. *Remote Sens.* **2017**, *9*, 270. [[CrossRef](#)]
29. Deng, Y.; Jiang, W.; Tang, Z.; Ling, Z.; Wu, Z. Long-term changes of open-surface water bodies in the Yangtze River Basin based on the Google Earth Engine cloud platform. *Remote Sens.* **2019**, *11*, 2213. [[CrossRef](#)]
30. Inman, V.L.; Lyons, M.B. Automated inundation mapping over large areas using Landsat data and Google Earth Engine. *Remote Sens.* **2020**, *12*, 1348. [[CrossRef](#)]
31. Jiang, C.; Chen, S.L.; Pan, S.; Fan, Y.S.; Ji, H.Y. Geomorphic evolution of the Yellow River delta: Quantification of basin-scale natural and anthropogenic impacts. *Catena* **2018**, *163*, 361–377. [[CrossRef](#)]
32. Fan, Y.S.; Chen, S.L.; Zhao, B.; Ji, H.Y.; Jiang, C. Monitoring tidal flat dynamics affected by human activities along an eroded coast in the Yellow River Delta. *Environ. Monit. Assess.* **2018**, *190*, 396. [[CrossRef](#)] [[PubMed](#)]
33. Kuenzer, C.; Ottinger, M.; Liu, G.H.; Sun, B.; Baumhauer, R.; Dech, S. Earth observation-691 based coastal zone monitoring of the Yellow River delta: Dynamics in China’s second largest 692 oil producing region observed over four decades. *Appl. Geogr.* **2014**, *55*, 92–107. [[CrossRef](#)]

34. Kong, X.L.; Li, Y.L.; Han, M.; Tian, L.X.; Niu, X.R.; Zhu, J.Q.; Wang, M.; Huang, S.P. Distribution of natural wetlands in the Yellow River Delta for three periods since 1990 and driving factors of their changes. *Wetl. Sci.* **2020**, *18*, 603–612.
35. Ren, M.E.; Cui, G. Relative sea-level rise in yellow river delta—Implications and response strategies. *J. Chin. Geogr.* **1991**, *5*, 85–95.
36. Li, C.; Li, G.E.; Xie, Z.W.; Wang, H.C. Analysis of the land use history and the causes in Yellow River Delta during the last 15 years. *Sci. Technol. Rev.* **2015**, *33*, 37–44. (In Chinese)
37. Fan, Y.S.; Dou, S.T.; Wang, G.Z.; Wang, K.R. Review and prospect of Yellow River estuary management. *Water Resour. Dev. Res.* **2022**, *22*, 48–53. (In Chinese)
38. Jia, M.M.; Wang, Z.M.; Mao, D.H.; Ren, C.Y.; Wang, C.; Wang, Y.Q. Rapid, robust, and automated mapping of tidal flats in China using time series Sentinel-2 images and Google Earth Engine. *Remote Sens. Environ.* **2021**, *255*, 112285. [[CrossRef](#)]
39. Liu, X.; Gao, Z.; Ning, J.; Yu, X.; Zhang, Y. An improved method for mapping tidal flats based on remote sensing waterlines: A case study in the Bohai Rim, China. *IEEE J. Sel. Top. Appl. Earth Obs. Remote Sens.* **2016**, *9*, 5123–5129. [[CrossRef](#)]
40. Liu, Y.; Li, M.; Mao, L.; Cheng, L.; Chen, K.F. Seasonal pattern of tidal-flat topography along the Jiangsu Middle Coast, China, using HJ-1 optical images. *Wetlands* **2013**, *33*, 871–886. [[CrossRef](#)]
41. Murray, N.J.; Phinn, S.R.; Clemens, R.S.; Roelfsema, C.M.; Fulter, R.A. Continental scale mapping of tidal flats across East Asia using the Landsat archive. *Remote Sens.* **2012**, *4*, 3417–3426. [[CrossRef](#)]
42. Zhu, Z.; Woodcock, C.E.; Holden, C.; Yang, Z. Generating synthetic Landsat images based on all available Landsat data: Predicting Landsat surface reflectance at any given time. *Remote Sens. Environ.* **2015**, *162*, 67–83. [[CrossRef](#)]
43. Luque, A.; Carrasco, A.; Martin, A.; Ana, D. The impact of class imbalance in classification performance metrics based on the binary confusion matrix. *Pattern Recognit.* **2019**, *91*, 216–231. [[CrossRef](#)]
44. Zhao, Y.; Xu, J.; Zhong, K.; Wang, Y.; Hu, H.; Wu, P. Impervious Surface Extraction by Linear Spectral Mixture Analysis with Post-Processing Model. *IEEE Access* **2020**, *8*, 128476–128489. [[CrossRef](#)]
45. Chi, Y.; Shi, H.; Sun, J.; Li, J.; Yang, F.; Fu, Z.Y. Spatio-temporal characteristics and main influencing factors of vegetation net primary productivity in the Yellow River Delta in recent 30 years. *Acta Ecol. Sin.* **2018**, *38*, 2683–2697. (In Chinese)
46. Zhou, X.; Xu, X. Typical models of efficient ecological fishery in Dongying City. *J. Shanghai Ocean Univ.* **2014**, *23*, 463–469. (In Chinese)
47. Xie, C.J.; Cui, B.S.; Xie, T.; Yu, S.; Shao, X. Hydrological connectivity dynamics of tidal flat systems impacted by severe reclamation in the Yellow River Delta. *Sci. Total Environ.* **2020**, *739*, 139860. [[CrossRef](#)]
48. Wang, Y. *Coastal Marine Scientific Research and Practice*; Nanjing University Press: Nanjing, China, 2021.
49. Ren, G.; Zhao, Y.; Wang, J.; Pw, A.; Yi, M.A. Ecological effects analysis of *Spartina alterniflora* invasion within yellow river delta using long time series remote sensing imagery. *Estuar. Coast. Shelf Sci.* **2020**, *249*, 207111. [[CrossRef](#)]
50. Li, Y.; Wu, H.; Zhang, S. Morphological characteristics and changes of tidal creeks in coastal wetlands of the Yellow River delta under *Spartina alterniflora* invasion and continuous expansion. *Wetl. Sci.* **2021**, *19*, 88–97.
51. Zhang, C.; Chen, S.; Li, P.; Liu, Q. Spatiotemporal dynamic remote sensing monitoring of typical wetland vegetation in the Current Huanghe River Estuary Reserve. *Haiyang Xuebao* **2022**, *44*, 125–136. (In Chinese)
52. Shi, H.; Lu, J.; Zheng, W.; Sun, J.; Ding, D. Evaluation system of coastal wetland ecological vulnerability under the synergetic influence of land and sea: A case study in the Yellow River Delta, China. *Mar. Pollut. Bull.* **2020**, *161*, 111735. [[CrossRef](#)] [[PubMed](#)]
53. Sun, J.; Chi, Y.; Fu, Z.; Li, T.; Dong, K. Spatiotemporal variation of plant diversity under a unique estuarine wetland gradient system in the Yellow River delta, China. *Chin. Geogr. Sci.* **2020**, *30*, 217–232. [[CrossRef](#)]
54. Wu, X.; Bi, N.; Xu, J.; Nittrouer, J.A.; Yang, Z.; Saito, Y.; Wang, H. Stepwise morphological evolution of the active Yellow River (Huanghe) delta lobe (1976–2013): Dominant roles of riverine discharge and sediment grain size. *Geomorphology* **2017**, *292*, 115–127. [[CrossRef](#)]
55. Bi, N.; Wang, H.; Wu, X.; Saito, Y.; Xu, C.; Yang, Z. Phase change in evolution of the modern Huanghe (Yellow River) Delta: Process, pattern, and mechanisms. *Mar. Geol.* **2021**, *437*, 106516. [[CrossRef](#)]
56. Viles, H.A.; Naylor, L.A.; Carter, N.E.A.; Chaput, D. Biogeomorphological disturbance regimes: Progress in linking ecological and geomorphological systems. *Earth Surf. Processes Landf.* **2008**, *33*, 1419–1435. [[CrossRef](#)]
57. Verheijen, B.; Varner, D.M.; Haukos, D.A. Effects of large-scale wetland loss on network connectivity of the Rainwater Basin, Nebraska. *Landsc. Ecol.* **2018**, *33*, 1939–1951. [[CrossRef](#)]